RSC Advances

ROYAL SOCIETY OF CHEMISTRY

www.rsc.org/advances

Up-conversion photoluminescence and temperature sensing properties of Er^{3+}-doped $Bi_4Ti_3O_{12}$ nanoparticles with good water-resistance performance

T. Wei[&,†], T. B. Zhang[&], Y. J. Ma[&], Y. F. Xie[&], C. Z. Zhao[$], F. M. Yang[&], H. Y. Xiao[&], Y. Zhao[&]

[&]*College of Science, Civil Aviation University of China, Tianjin 300300, China*

[$]*School of Electronics and Information Engineering, Tianjin Polytechnics University, Tianjin 300160, China*

Abstract

Er^{3+}-doped $Bi_4Ti_3O_{12}$ (BiT-x) with different particle sizes were successfully synthesized via a low-cost coprecipitaton method without any surfactants. The phase and structure were characterized by X-ray diffraction (XRD) and analyzed using Rietveld structural refinements. The morphologies were characterized by scanning electron microscope (SEM). We show that synthesis temperature plays an important role to determine the phase and particle size of BiT-x. As a function of excitation power, it is proved that the obtained BiT-x samples display size-dependent up-conversion (UC) luminescence properties. Meanwhile, with x increase, manipulation of UC emission is observed which can be illustrated by the increased CR

[†] Corresponding Author, E-mail: weitong.nju@gmail.com or weitong_nju@163.com

process probability. The critical energy transfer distance (R_c) and the major interaction mechanism among Er^{3+} ions are also determined. Furthermore, the temperature sensing behavior based on fluorescence intensity ratio (FIR) technique from the thermally coupled $^2H_{11/2}$ and $^4S_{3/2}$ levels are studied in the temperature range from 115 K to 490 K. It is found that the maximum sensing sensitivity is $0.0043K^{-1}$. Meanwhile, BiT-0.05 nanoparticles also display good water-resistance feature. These results reveal that BiT-x oxides may have promising applications in future optical temperature sensors.

Keywords: Bismuth layer-structured ferroelectric; Luminescence; Nanoparticles

1. Introduction

Near-Infrared-to-visible (NIR-VIS) up-conversion (UC) photoluminescence is a typical nonlinear process in which two or more lower-energy photons (NIR) are converted into one emitted higher-energy photon (VIS).[1-6] Considerable interest has been centered on the field of UC photoluminescence inspired by the potential applications in three dimensional displays, illuminating system, solid-state lasers, biomedicine, thermometry and anti-counterfeit markers.[1-6] Up to now, a lot of UC host materials have been developed and studied. Fluorides and chlorides are the popular UC hosts owing to the low phonon energy. Unfortunately, the poor physical and chemical stabilities and pollution to environment of fluorides and chlorides restrict their real applications.[7]

Alternatively, oxides have been marked as efficient matrices for rare-earth (RE) ions doping because of their lower toxicity and desirable chemical stability and durability. Among these oxides, bismuth layer-structured ferroelectric (BLSF) oxide, a group of important and interesting host, has been regarded as a promising host for UC applications.[10,13-18] Therefore, various BLSF-based UC compounds have been developed, such as Er-doped $CaBi_2Ta_2O_9$, Er doped $Bi_4Ti_3O_{12}$-$SrBi_4Ti_4O_{15}$, Li- and Ho-codoped $CaBi_4Ti_4O_{15}$, etc.[13-18] However, previous works mainly focused on the UC feature of ceramic samples. Hitherto, there is relatively little work focusing on UC properties of BLSF nanoparticles. As modern electronic devices are being reduced in size, the development of UC materials with particle size in the nanometer regime has become pivotal. Therefore, further work is necessary to synthesize suitable BLSF-based UC nanoparticles (UCNPs) and study their UC properties in detail which will be

in favor of the prehension of size-dependent UC mechanism for this type of inorganic host.

On the other hand, as a unique class of optical materials, UCNPs can also be utilized in biological sensing. Because biological process is temperature dependent, accurate determination of intracellular temperature is significant for the disease diagnose and therapy.[20-27] For this purpose, conventional temperature sensors based on the principle of liquid and metal expansion cannot be applied. In contrast, fluorescence intensity ratio (FIR) technique of UCNPs, which utilizes temperature-dependent UC intensity ratio from two thermally coupled energy levels of RE ions, has received great attention and is regarded as a promising method for temperature sensing in biology.[20-27] Much attention has been focused on designing small size optical temperature sensor with high sensitivity. However, up to now, investigations on temperature sensing performances of the BLSF-based UCNPs are still scant. As well known, the sensitivity of the previous temperature sensing materials is still low for the practical application. Therefore, it is an urgent task to develop new proper host materials (such as BLSF) in order to improve the sensitivity.

In this instance, a typical BLSF compound, $Bi_4Ti_3O_{12}$ (BiT), possessing with desirable chemical stability and relatively low phonon energy (~800cm^{-1}), has been proved to be a perfect UC host and is currently selected as the host matrix in this work.[10,13-18] For UC designing, Er^{3+} ion, involving a rich and ladder-like electronic energy level structure, is exploited as the luminescent active ion. Meanwhile, for Er^{3+}, electron population in the adjacent thermally coupled levels (TCL), $^2H_{11/2}$ and $^4S_{3/2}$, displays ingenious response to temperature, which can be responsible for temperature sensing based on FIR technique. Furthermore, apart from complex and expensive synthesis process of UCNPs, we prepare a

series of Er^{3+}-doped BiT (BiT-x) UCNPs through a simple and low-cost coprecipitaton method. The crystal structure, UC photoluminescence, temperature sensing behavior, and water-resistance properties of BiT-x are discussed in detail.

2. Experimental detail

A series of BiT-x samples ($0 \leq x \leq 0.2$) were prepared by a coprecipitaton method. Bismuth nitrate ($Bi(NO_3)_3 \cdot 5H_2O$, 99%) was supplied by Sinopharm Chemical Reagent Beijing Co., Ltd. Titanium Butoxide ($C_{16}H_{36}O_4Ti$, 99%) and Erbium nitrate ($Er(NO_3)_3 \cdot 5H_2O$, 99.9%) were supplied by Aladdin Industrial Corporation. All chemicals were used as the starting materials without further purification. Stoichiometric $Bi(NO_3)_3 \cdot 5H_2O$ was dissolved in dilute nitric acid with constant stirring until all powders completely dissolved to get the bismuth nitrate solution. Erbium nitrate solution was obtained by dissolving $Er(NO_3)_3 \cdot 5H_2O$ in distilled water with constant stirring. Then, Erbium nitrate solution was added to bismuth nitrate solution with stirring for 60min to form a Bi and Er mixed solution. $C_{16}H_{36}O_4Ti$ solution was obtained by dissolving $C_{16}H_{36}O_4Ti$ in ethanol with constant stirring for 30min. Subsequently, $C_{16}H_{36}O_4Ti$ solution was added to the above Bi and Er mixed solution with stirring for 60min. Then, the pH value of the solution was adjusted to about 9 by adding ammonia water along with slurry-like white colloidal precipitates. The obtained precipitates were washed with distilled water for several times. Finally, the washed precipitates were dried and sintered at different temperatures for 90 min. Furthermore, $Y_{1.98}Er_{0.02}O_3$ (Y_2O_3: Er) samples were synthesized by co-precipitation followed by thermal treatment method.

$Y(NO_3)_3 \cdot 6H_2O$ (99.9%) and $Er(NO_3)_3 \cdot 6H_2O$ (99.9%) were selected as starting materials, and ammonia water as precipitant. Appropriate amounts of $Y(NO_3)_3 \cdot 6H_2O$ and $Er(NO_3)_3 \cdot 6H_2O$ were dissolved in deionized water under condition of stirring. Then, ammonia solution was dropwise added to the above mixture. Then, the precipitates were washed and dried at 100^oC for 12h. The resultant powders were reground, then, calcined at 600 ^oC for 2 hours and sintered at 850 ^oC for 2 hours. The obtained Y_2O_3: Er samples were utilized for the following UC luminescence measurements.

The phase identification was determined by an X-ray powder diffractometer (XRD) (X'pert-MPD, Philips) using Cu Kα radiation, with working current and voltage of 40 mA and 40 kV, respectively. XRD measurements were carried out over an angular range from 5^0 to 120^0 with scanning step of 0.02^0. The general structure analysis system (GSAS) program was used for Rietveld structural refinement.[28-29] For UC luminescence measurement, a 980 nm power-controllable NIR diode laser (Hi-Tech Optoelectronics Co., Ltd) with a maximum power of 2 W was used to pump the BiT-x samples. The UC luminescence spectra were collected under the same experimental conditions for all BiT-x samples by a Zolix SBP300 spectrofluorometer (SBP300, Zolix Instruments Co. Ltd) with a photo-multiplier tube (PMT) as the detector. The signals were recorded using the data acquisition system connected to a computer. For variable temperature UC measurements, the temperature of the samples, ranging from 115K to 490 K, was controlled using a temperature-controlled stage (Cryo-77). The fourier transform infrared (FT-IR) spectra were recorded on samples in KBr tablets using a FT-IR spectrophotometer (Nicolet, America). The water resistance samples were fabricated by the following procedure. The nanoparticles for water resistance measurements were

dispersed in distilled water (30 ml) by sonication and magnetic stirring for 30 min. Then, the dispersed nanoparticles were hold in distilled water for 0, 20 h, 40 h, 70 h, and 90 h, respectively. Afterwards, the as-prepared nanoparticles were dried at 100 ^{o}C.

3. Results and discussion

3.1 Structural characterization

The phases and structures of all BiT samples were characterized by XRD analyses. Fig. 1 gives the representative XRD patterns of BiT-0 and BiT-0.08 synthesized at different temperatures for 90 min. From the diffractograms, it is found that synthesis temperature plays a crucial factor on controlling the formation of phase. The XRD patterns show remarkable temperature dependence. With temperature increase, the appearance of sharp diffraction peaks in Fig. 1 indicates the good crystallization of BiT-x samples. Moreover, temperature also determines the phase purity. The XRD patterns of BiT-0 and BiT-0.08 synthesized at 500 ^{o}C reveal some diffraction peaks which stem from impurity $Bi_2Ti_2O_7$. Starting from 600 ^{o}C, the X-ray diffraction peaks of BiT-x match well with the Joint Committee for Powder Diffraction Standards card (No. 56-0814) and the main diffraction peaks are indexed as shown in Fig. 1.[16] The highest diffraction peak is (117) which is consistent with the observations that the strongest diffraction corresponds to (112*m+1) reflection in the Aurivillius phase BLSF materials.[13] The obtained BiT-x samples possess typical bismuth Aurivillius type structure with m=3. Within the apparatus resolution limit, no other

non-bismuth-layered perovskite structures or secondary phase emerge, indicating that Er^{3+} ions completely dissolved in BiT host lattice. The above XRD results suggest that BiT-x samples crystallize in the polar orthorhombic phase, with space group Fmmm. Furthermore, normalized monolog XRD plots of BiT-0 and BiT-0.08 ranging from 28.5^0 to 32.5^0 are presented in Fig. 2. Obvious broadening of diffraction peaks can be found with decreasing of synthesis temperature, which indicates the continuous reduction of particle size. To inspect the particle size and morphology, SEM measurements were carried out. Fig. 3 displays the SEM micrographs of BiT-0. The particle size locates at nano-scaled level when temperature is lower than 800 ^{o}C. The average particle size is about 50, 100, and 200 nm when synthesis temperature is 500, 600, and 700 ^{o}C, respectively. However, obvious enhancement of particle size emerges when temperature is 800 ^{o}C. Micro-scaled particles (about 2μm) can be obtained as indicated in Fig. 3(d). In addition, Fig. S1 provides the SEM micrographs of BiT-x (x=0.02, 0.05, 0.08, and 0.15) synthesized at 700 ^{o}C. Relatively homogeneous particle morphology is observed for each sample which alludes the monophase constitution. Meanwhile, we can also see that the particle size shows no obvious variation with x increase.

Furthermore, to obtain meticulous information on structural parameters, we consult to the Rietveld structural refinement. The measured XRD patterns and Rietveld refinement results for BiT-0, BiT-0.05, and BiT-0.2 nanoparticles synthesized at 700 ^{o}C are given in Fig. 4. The coordinates of BiT were used as an initial model. Fig. 4 presents that the final Rietveld refinement profiles match well with the measured XRD patterns. The reliability factors, experimental conditions, and the refined lattice parameters are listed in Table 1. The reliability factors, R_p and R_{wp}, are 3.71% and 4.94% for BiT-0, 3.88% and 5.15% for

BiT-0.05, and 4.03% and 5.26% for BiT-0.2, respectively. The refined lattice parameters are a=5.41195 (10) Å, b=5.44646 (10) Å, c=32.8075 (8) Å, and V_{unit}=967.032 (37) $Å^3$ for BiT-0, a=5.40867 (10) Å, b=5.44238 (10) Å, c=32.8007 (7) Å, and V_{unit}=965.523 (36) $Å^3$ for BiT-0.05, while a=5.40482 (16) Å, b=5.43065 (16) Å, c=32.7991 (11) Å, and V_{unit}=962.706 (58) $Å^3$ for BiT-0.2, suggesting the lattice shrinkage of BiT-x with x increase. Referring to the ion radii of Bi^{3+}(1.38 Å, CN12) and Er^{3+} (1.23 Å, CN12),[15,30] the variation of crystal lattice parameters induced by the doping of Er^{3+} at Bi^{3+} site can be understood. Furthermore, Tables S1-S3 list the atomic coordinates, isotropic thermal parameters, and atomic occupancies of BiT-0, BiT-0.05, and BiT-0.2 samples. It is obtained that Er^{3+} mainly substitutes the perovskite A-site Bi^{3+}(Bi1, 8i-site), which is consistent with previous investigations.[16]

3.2 UC photoluminescence

Fig. 5 gives the UC spectra of BiT-0.08 excited through a NIR 980 nm diode laser at room temperature. The UC spectra of BiT-0.08 are mainly dominated by two green emissions and a red emission. The intense UC green emissions peaking at 525 and 549 nm are assigned to intra-*4f* $^2H_{11/2}\rightarrow{}^4I_{15/2}$ and $^4S_{3/2}\rightarrow{}^4I_{15/2}$ electronic transitions of Er^{3+} ion, respectively. The weak UC red emission, situating at around 630–690 nm region, originates from $^4F_{9/2}\rightarrow{}^4I_{15/2}$ transition.[1-6,13-18] The bright UC green emission of BiT-0.08 can be easily observed by the naked eye at room temperature as shown in the inset of Fig. 5(a). Particularly, it is found that the UC emission intensities are distinctly enhanced when the synthesis temperature changes from 500 to 800 °C. To clearly view, the integral intensities of UC green and red emissions

versus synthesis temperature (t) are plotted in Figs. 5(b) and 5(c). It is observed that UC green and red emissions are both enhanced dramatically with increasing of t. However, the increased magnitude of UC green intensity is larger than that of UC red intensity. The UC green and red intensities of the sample sintered at 700 °C are respectively 54 and 19 times higher than that of the sample sintered at 500 °C. Thus, the relative intensity ratio of red to green ($R_{R/G}$) in Fig. 5(d) displays monotonous reduction with t increase. In addition, to evaluate the UC emission, the UC luminescence comparison between Y_2O_3: Er and BiT-0.08 (sintered at 700 °C) is given in the inset of Fig. 5(b) which indicates the strong UC emission of BiT-0.08. Moreover, the inset in Fig. 5(d) gives the FT-IR spectra of BiT-0.08 synthesized at 600 and 800 °C, which clearly presents several characteristic absorption bands. Two strong bands at about 580cm^{-1} and 820cm^{-1} relate with the stretching vibrations of Ti-O and Bi-O, respectively, which indicates the formation of BLSF phase.[31] The bands at about 3400cm^{-1} and 1600cm^{-1} can be attributed to OH bending and stretching vibrations.[31-32] The weak peak at about 2300 cm^{-1} belongs to the stretching vibrations of C=O.[31-32] It can be seen that the bands at 3400cm^{-1}, 2300 cm^{-1}, and 1600cm^{-1} are sharply reduced when t=800 °C, indicating that most of organic ligands are removed.

Fig. 6 presents the UC spectra of UCNPs for BiT-x samples with different x at room temperature. The UC green emissions origin from $^2H_{11/2}\rightarrow{}^4I_{15/2}$ and $^4S_{3/2}\rightarrow{}^4I_{15/2}$ transitions, while the UC red emission corresponds with $^4F_{9/2}\rightarrow{}^4I_{15/2}$ transition of Er^{3+}. With x increase, UC green emission intensity increases first and then decreases as revealed in Fig. 6(b). This result shows that the optimal doping concentration of Er^{3+} in BiT host is 0.05 which is consistent with other UCNPs system.[1-6] The UC green emission intensity therewith decreases

when Er^{3+} concentration exceeds the critical concentration owing to the concentration quenching effect which can be illustrated by the critical energy transfer between the nearest Er^{3+} ions. However, different variation trend is obtained for UC red emission intensity in Fig. 6(c) which reflects a continuous augment. Accordingly, the $R_{R/G}$ value presented in Fig. 6(d) displays a monotonous enhancement. In addition, the chromaticity coordinates were calculated from the UC spectra by the method using the 1931 CIE (Commission Internationale de l'Eclairage, France) system. Fig. 7 shows that the obtained CIE chromaticity coordinates are x=0.236 and y=0.740, x=0.251 and y=0.727, x=0.281 and y=0.699 for BiT-0.02 (a), BiT-0.08 (b), and BiT-0.2 (c), respectively. It illuminates the red shifting of the UC emission with x increase which matches well with their corresponding real emission spectra. It is noted that different populating paths of Er^{3+} induce the variation of relative intensity of different transitions and will be described in the later section of this paper.

The critical energy transfer distance (R_c) can be calculated using the concentration quench relation proposed by Blasse:

$$R_c \approx 2\left(\frac{3V}{4\pi x_c N}\right)^{1/3} \quad (1)$$

where x_c is the critical concentration of the activator ion (Er^{3+}), N is the number of chemical formula in the unit cell, and V is the volume of the unit cell.[33-35] For BiT-x, the unit cell volume of BiT-0.05 is 965.523 (36) $Å^3$. x_c is determined as 0.05. N is adopted as 4. Using these values, the obtained R_c value is about 20.97 Å. Furthermore, to obtain the interaction type between Er^{3+} ions in BiT-x, the equation proposed by Dexter can be used:

$$\frac{I}{x} = K\left[1 + \beta(x)^{\theta/3}\right]^{-1} \quad (2)$$

where I is the UC emission intensity, x is the activator concentration, K and β are constants at

the same excitation condition for a given host. θ is 3 for the exchange interaction among the nearest-neighbor ions, while it takes 6, 8, and 10 values which corresponds to dipole-dipole (d-d), dipole-quadrupole (d-q), quadrupole-quadrupole (q-q) interactions, respectively.[36] Fig. 8 gives that the dependence of lg(I/x) on lgx for the UC green emission is linear and the slope is about -1.4. Therefore, the value of θ can be calculated as 4.2, which is between 3 and 6, indicating that the major interaction mechanism for present BiT-x system can be attributed to the superposition interaction of the exchange and d-d interaction.[36]

To determine the number of photons involved in the UC process of BiT-x, the UC luminescence intensity (I) was measured as a function of the pump laser power (P). For the unsaturated UC process, it is believed that I depends on P following the relationship as follows:[1-6,13-18]

$$I \propto P^n, \qquad (3)$$

where P is the power of pumping laser, I is the output UC intensity, and n is the absorbed photon numbers per UC emission photon which can be calculated from the slope of the *lg (I)* versus *lg (P)* fitting. Fig. 9 displays the logarithmic plots for the integrated UC green (from 500-580 nm) and red (from 630 to 690 nm) emission intensities of BiT-0.08 as function of power. The linear fitting slopes for ($^2H_{11/2}$, $^4S_{3/2}$) $\rightarrow {}^4I_{15/2}$ and $^4F_{9/2} \rightarrow {}^4I_{15/2}$ transitions are calculated in Fig. 9. The values of n are determined to be 1.73±0.02, 1.71±0.02, 1.50±0.01, and 1.33±0.02 for UC green emissions of BiT-0.08 with particle size of 50, 100, 200, and 2μm, respectively. For UC red emissions, the corresponding values of n are 1.78±0.04, 1.75±0.03, 1.54±0.02, and 1.41±0.02, respectively. Obviously, it is found that the values of n decrease with increasing of particle size. As well known, the population of UC green and red

levels comes from a two-photon process and the value of n should be close to 2.[13-18] However, it is found that the obtained n values for BiT-0.08 with larger particle size greatly deviate from the typical value of 2 for the two-photon UC population process. This phenomenon is mainly attributed to the saturation effect, originating from the competition between linear decay and UC processes for the depletion of the intermediate excited states which has been theoretically proved by Pollnau et al.[37-38] For BiT-0.08, the degree of saturation is lower for samples with smaller particle size since the linear decay process would increase owing to the increase of nonradiative relaxation processes along with the decreasing of particle size. Furthermore, the linear fitting results of *lgI-lgP* plots are presented in Fig. S2 for BiT-x samples synthesized at 700 ^{o}C. The values of n are calculated to be 1.70±0.01, 1.61±0.01, 1.50±0.01, 1.46±0.01, and 1.35±0.02 for UC green emissions of BiT-x with x=0.02, 0.05, 0.08, 0.15, and 0.2, respectively. For UC red emissions, the corresponding values of n are deduced to be 1.64±0.03, 1.63±0.02, 1.54±0.02, 1.42±0.02, and 1.33±0.01, respectively. It is obtained that the values of n both increase with x decrease for UC green and red transitions. Obvious saturation effect is observed for BiT-0.2 in which the values of n are much smaller than 2. This phenomenon should be related with the concentration of Er^{3+} ions and may be attributed to the interaction among Er^{3+} ions at high concentration.[38] Thus, it is indicated that the concentration of Er^{3+} ions also has an influence on the competition between linear decay and UC processes for the depletion of the intermediate excited states.

Fig. 10 shows the energy level diagram and the UC mechanisms. Under 980 nm excitation, Er^{3+} ions on the ground state $^4I_{15/2}$ are excited to the long-lived excited state $^4I_{11/2}$ through ground state absorption (GSA, $^4I_{15/2}$+ photon→ $^4I_{11/2}$). Then, some Er^{3+} ions on the

$^4I_{11/2}$ level are further excited to $^4F_{7/2}$ state via excited state absorption (ESA1, $^4I_{11/2}$+ photon→ $^4F_{7/2}$) and ETU1 ($^4I_{11/2}$+ $^4I_{11/2}$→ $^4F_{7/2}$+ $^4I_{15/2}$) processes. Subsequently, $^2H_{11/2}$ and $^4S_{3/2}$ levels are populated by efficiently nonradiative relaxation from the upper $^4F_{7/2}$ level owing to the small energy gap between these levels. Finally, $^2H_{11/2}$ → $^4I_{15/2}$ and $^4S_{3/2}$ → $^4I_{15/2}$ transitions give the UC green emissions peaked at 525 and 549nm, respectively. For the UC red emission, it comes from $^4F_{9/2}$ → $^4I_{15/2}$ transition of Er^{3+}. The $^4F_{9/2}$ level can be populated by two possible routes. First, some Er^{3+} ions on the $^4I_{11/2}$ level will nonradiativly relax to $^4I_{13/2}$ state. Then, the $^4F_{9/2}$ level is populated by ESA2 ($^4I_{13/2}$+ photon→ $^4F_{9/2}$) and ETU2 ($^4I_{11/2}$+ $^4I_{13/2}$→$^4I_{15/2}$+ $^4F_{9/2}$) processes. Second, the electrons coming from the nonradiative relaxation of $^4S_{3/2}$ excited state can also populate the $^4F_{9/2}$ level. It is believed that large energy gaps of $^4I_{11/2}$ and $^4I_{13/2}$ (~ 3620cm^{-1}), $^4S_{3/2}$ and $^4F_{9/2}$ levels (~ 3080 cm^{-1}) are relatively unfavorable for the nonradiative relaxations of $^4I_{11/2}$ to $^4I_{13/2}$ and $^4S_{3/2}$ to $^4F_{9/2}$. Therefore, the UC green emission is dominant compared with that of red emission. However, with particle size decrease, a number of surface defects with available large vibrational modes (eg. OH, C=O) are involved due to the elevation of surface to volume ratio as confirmed in the inset in Fig. 5(d). These surface defects (OH and C=O) can easily bridge the energy gaps of $^4I_{11/2}$ and $^4I_{13/2}$ (~ 3620cm^{-1}), $^4S_{3/2}$ and $^4F_{9/2}$ levels (~ 3080 cm^{-1}) by one or two phonons. This would efficiently increase the nonradiative relaxation probability of $^4I_{11/2}$ →$^4I_{13/2}$ and $^4S_{3/2}$ →$^4F_{9/2}$ transitions. It is consistent with the increment of $R_{R/G}$ with reducing of particle size as shown in Fig. 5. On the other hand, with increasing the contents of Er^{3+} (x), the distance among Er^{3+} ions decreases gradually, and the cross relaxation (CR) process probability is enhanced which would tailor the UC spectra as described previously.[39-41] The CR1 process would suppress the

population on $^4F_{7/2}$ and increase the population on $^4F_{9/2}$ level. The CR2 process reduces the population in $^4S_{3/2}$ state, and elevates the population in $^4I_{13/2}$ level. Then, the $^4F_{9/2}$ level is further populated by ESA2 and ETU2 processes. Thus, with x increase, these two CR processes given in Fig. 10 can effectively populate the $^4F_{9/2}$ level which improves the UC red emission intensity and simultaneously reduces the UC green emission intensity, leading to the relative increment of the red intensity as revealed in Fig. 6.

3.3 Temperature sensing behavior

Fig. 11 shows the UC emission spectra of the optimal BiT-0.05 UCNPs (prepared at 700 ^oC) under various temperatures from 115K to 235K. It is worth noting that the power density is relatively low and adopted as 0.3W/cm^2 in order to reduce the heating effect caused by laser excitation. From Fig. 11, it is detected that the positions of the UC emission bands barely change with increasing of temperature. However, it is interestingly found that the intensities of the two green emission bands ($^2H_{11/2} \rightarrow {}^4I_{15/2}$ and $^4S_{3/2} \rightarrow {}^4I_{15/2}$) of Er^{3+} vary in an opposite way with temperature increase, whereas the intensity of red emission band nearly remains the same. In addition, it is noted that the green emission ($^2H_{11/2} \rightarrow {}^4I_{15/2}$) cannot be observed as temperature below 145K, indicating the difficulty to populate the $^2H_{11/2}$ state from $^4S_{3/2}$ level by thermal excitation at low temperature.

For Er^{3+} ion, it is known that the energy gap between $^2H_{11/2}$ and $^4S_{3/2}$ levels is about 800cm^{-1}. The relatively small gap permits that the state of $^2H_{11/2}$ could be populated from $^4S_{3/2}$ level by thermal excitation. The population on these two levels follows a Boltzmann

distribution, which leads to an obvious change in the emission intensities of $^2H_{11/2} \rightarrow {}^4I_{15/2}$ and $^4S_{3/2} \rightarrow {}^4I_{15/2}$ with temperature increase. Therefore, the response of FIR from the two thermally coupled energy levels ($^2H_{11/2}$ and $^4S_{3/2}$) to temperature can be utilized for the temperature sensor by using the following equation,[20-27]

$$FIR = R = \frac{I_H}{I_S} = \frac{N\left(^2H_{11/2}\right)}{N\left(^4S_{3/2}\right)} = \frac{c_1(\nu)A_1 g_1 h\nu_1 \beta_1}{c_2(\nu)A_2 g_2 h\nu_2 \beta_2} exp\left(\frac{-\Delta E_{HS}}{k_B T}\right) = Cexp\left(\frac{-\Delta E_{HS}}{k_B T}\right) \quad (4)$$

where I_H and I_S are the integrated intensities for $^2H_{11/2} \rightarrow {}^4I_{15/2}$ and $^4S_{3/2} \rightarrow {}^4I_{15/2}$, respectively. $N(^2H_{11/2})$ and $N(^4S_{3/2})$ represent the population numbers of the $^2H_{11/2}$ and $^4S_{3/2}$ levels. The values of $c_i(\nu)$ are related to the response of the detection system. The factors, A_i, g_i, $h\nu_i$, and β_i, respectively correspond with the spontaneous radiative rate, the degeneracy, the photon energy, and the branching ratio of fluorescence transitions from the $^2H_{11/2}$ and $^4S_{3/2}$ levels to the $^4I_{15/2}$ level.[20-27] C is the proportionality constant. ΔE_{HS} is the energy gap between the $^2H_{11/2}$ and $^4S_{3/2}$ levels. k_B is the Boltzmann constant and T is the absolute temperature. Fig. 12(a) gives the temperature-dependent UC green emission ranging from 115K to 490K in which the spectra are normalized to the emission peak at 549 nm. With temperature increase, the emission intensity of $^2H_{11/2}$ level increases continuously with respect to the $^4S_{3/2}$ level. The energy gap between $^2H_{11/2}$ and $^4S_{3/2}$ levels can be obtained from the UC spectra and is about 832cm^{-1} (24 nm). Fig. 12(b) presents a natural logarithm plot of the FIR for UC green emissions at 525 and 549 nm as a function of inverse absolute temperature in the range of 175 to 490 K. The experimental data can be fitted by a straight line with slope of about 1123. The calculated energy gap ΔE_{HS} is about 780cm^{-1} which is approximately equal to the experiment value of 832cm^{-1}. The temperature dependence of FIR in the range of 175 to 490K is described in Fig. 12(c). The value of FIR increases monotonously from 0.015 to

1.15 with the increment of temperature and reaches maximum when temperature is 490K. The experimental data given in Fig. 12(c) can be properly described by an exponential curve according to the results of the linear fitting. Furthermore, for temperature sensing applications, sensor sensitivity (S) is a crucial parameter for judging the sensor. The value of S can be calculated by the equation as follows:[20-27]

$$S = \frac{d(R)}{d(T)} = \frac{c_1(v)A_1g_1h\nu_1\beta_1}{c_2(v)A_2g_2h\nu_2\beta_2} exp\left(\frac{-\Delta E_{HS}}{k_BT}\right)\left(\frac{\Delta E_{HS}}{k_BT^2}\right) = R\left(\frac{\Delta E_{HS}}{k_BT^2}\right) \quad (5)$$

The corresponding resultant curve of S as a function of temperature is shown in Fig. 12(d). With temperature increase, the value of S gradually increases and reaches the maximum value of about 0.0043K^{-1} at 490K. In comparison with other temperature sensing materials, such as Yb-Er: $NaYF_4$, Yb-Er: $Na_{0.5}Bi_{0.5}TiO_3$, Er-Ho: Fluoroindate glass, etc,[42-44] the temperature sensitivity for BiT-0.05 has been promoted. It is indicated that BiT-0.05 is a promising temperature sensing material which may have a potential application in future optical temperature sensor.

3.4 Water-resistance performance

It is noted that the water resistance feature is another momentous performance which affects the practical application of UC materials in the extreme environment.[12-13] The reduction of luminescent performance has been detected in some materials after water treatment owing to hydrolysis. For Eu^{2+}-doped $SrAl_2O_4$ materials, the luminescent intensity decreases rapidly as water treatment time increases.[45] Similar decay behaviors of the luminescent intensity were also found in Mn^{2+}-doped ZnS and Eu^{2+}- and Dy^{3+}-doped $SrAl_2O_4$

materials.[46-47] Poor water resistance characteristic severely limits the application of these luminescent materials. It is worth noting that the materials used for optical temperature sensor should also possess good water resistance stability, which is important for the practical temperature sensing application in various surroundings. Therefore, Fig. 13 presents the water-resistance behavior of BiT-0.05 which was measured at room temperature. It is found that the emission intensity and shape of UC spectra display no obvious change under different immersion times. The inset of Fig. 13 gives the dependence of the UC integrated intensity between 450nm and 750nm wavelength region on immersion time. The UC integrated intensity gives a very weak dependence on immersion time and almost maintains the same UC integrated intensity as obtained before immersion. It is indicated that BiT-0.05 involves good water-resistance properties of UC luminescence which may have a potential application in the aqueous surroundings.

4. Conclusion

In summary, a simple low-cost coprecipitaton route is provided for facile synthesis of a series of BiT-x UCNPs. It is detected that synthesis temperature plays an important role to determine the phase and particle size of BiT-x. Under 980 nm excitation, size-dependent UC luminescence indicates that $R_{R/G}$ continuously increases with decreasing particle size, which is ascribed to the surface effect. Meanwhile, it is found that the slope in the *lgI-lgP* plot presents evident size-dependence and displays gradual reduction with increasing particle size for both UC green and red emissions, which is attributed to the saturation effect originating from the competition between linear decay and UC processes for the depletion of the

intermediate excited states. Moreover, with x increase, red shifting of the UC emission can be illustrated by the increased CR processes probability. The critical energy transfer distance (R_c) is about 20.97 Å and the major interaction mechanism between Er^{3+} ions can be attributed to the superposition interaction of the exchange and d-d interaction. Furthermore, temperature sensing behaviors based on the FIR technique from the thermally coupled $^2H_{11/2}$ and $^4S_{3/2}$ levels of Er^{3+} ions are also investigated in the temperature range from 115 K to 490 K. It is found that the maximum sensing sensitivity is $0.0043K^{-1}$. Meanwhile, it is interesting that BiT-0.05 nanoparticles also display good water-resistance feature. These results revealed that BiT-x oxides may have promising applications in future optical temperature sensors.

Acknowledgments

The authors gratefully acknowledge financial support from the Natural Science Foundation of China (No. 61504094), Tianjin Research Program of Application Foundation and Advanced Technology (No. 14JCQNJC03700), the National Undergraduate Training Programs for Innovation and Entrepreneurship (No. 201510059011), the Undergraduate Training Programs for Innovation and Entrepreneurship of Civil Aviation University of China (No. IECAUC2015029).

References:

1 F. Auzel, Chem. Rev., 2004, 104, 139.

2 J. C. Boyer, L. A. Cuccia and J. A. Capobianco, Nano. Lett., 2007, 7, 847.

3 Y. Liu, D. Tu, H. Zhu and X. Chen, Chem. Soc. Rev., 2013, 42, 6924.

4 F. Wang, Y. Han, C. S. Lim, Y. H. Lu, J. Wang, J. Xu, H. Chen, C. Zhang, M. Hong and X. Liu, Nature., 2010, 463, 1061.

5 G. Y. Chen, H. L. Qiu, P. N. Prasad and X. Y. Chen, Chem. Rev., 2014, 114, 5161.

6 B. Dong, D. P. Liu, X. J. Wang, T. Yang, S. M. Miao and C. R. Li, Appl. Phys. Lett., 2007, 90, 181117.

7 W. J. Kong, J. N. Shan and Y. G. Ju, Mater. Lett., 2010, 64, 688.

8 J. Hao, Y. Zhang and X. Wei, Angew. Chem. Int. Ed., 2011, 50, 6876-6880.

9 E**.** Cavalli, A. Belletti, R. Mahiou and P. Boutinaud, J. Lumin., 2010, 130, 733-736.

10 F. Gao, G. Ding, H. Zhou, G. Wu, N. Qin and D. Bao, J. Appl. Phys., 2011, 109, 043106.

11 T. Wei, X. D. Wang, C. Z. Zhao, M. F. Liu and J. M. Liu, Appl. Phys. Lett., 2014, 104, 261908.

12 Q. Zhang, K. Chen, L. Wang, H. Sun, X. Wang and X. Hao, J. Mater. Chem. C., 2015, 3, 5275.

13 P. Xiao, Y. Guo, M. Tian, Q. Zheng, N. Jiang, X. Wu, Z. Xia and D. Lin, Dalton Trans., 2015,44, 17366-17380.

14 D. Peng, X. Wang, C. Xu, X. Yao, J. Lin and T. Sun, J. Appl. Phys., 2012, 111, 104111.

15 T. Wei, X. D. Wang, C. Z. Zhao, T. B. Zhang, F. M. Yang, W. B. Wang and Y. J. Ma,

Ceram. Int., 2015, 41, 12364-12370.

16 R. Bokolia, O. P. Thakur, V. K. Rai, S.K.Sharma and K.Sreenivas, Ceram. Int., 2015, 41, 6055-6066.

17 T. Wei, C. P. Li, Q. J. Zhou, Y. L. Zou and L. S. Zhang, Mater. Lett., 2014, 118, 92.

18 H. Zou, X. Wang, Y. Hu, X. Zhu, Y. Sui and Z. Song, AIP. Adv., 2014, **4**, 127157.

19 J. S. Zhu, D. Su, X. M. Lu, H. X. Qin, Y. N. Wang, D. Y. Wang, H. L. W. Chan, K. H. Wong and C. L. Choy, J. Appl. Phys., 2002, 92, 5420.

20 P. V. dos Santos, M. T. de Araujo, A. S. Gouveia-Neto, J. A. Medeiros Neto and A. S. B. Sombra, Appl. Phys. Lett., 1998, **73**, 578.

21 W. Xu, Z. G. Zhang and W. W. Cao, Opt. Lett., 2012, 37, 4865–4867.

22 B. Dong, B. Cao, Y. He, Z. Liu, Z. Li and Z. Feng, Adv. Mater., 2012, 24, 1987.

23 L. H. Fishcher, G. S. Harms and O. S. Wolfbeis, Angew. Chem., 2011, 50, 4546.

24 P. Du, L. Luo, W. Li, Q. Yue and H. Chen, Appl. Phys. Lett., 2014, 104, 152902.

25 H. Zou, X. Wang, Y. Hu, X. Zhu, Y. Sui and Z. Song, AIP. Adv., 2014, 4, 127157.

26 L. Li, C. Guo, S. Jiang, D. K. Agrawalc and T. Li, RSC Adv., 2014, 4, 6391.

27 Y. Tian, B. Tian, C. Cui, P. Huang, L. Wang and B. Chen, RSC Adv., 2015, 5, 14123.

28 B. H. Toby, J. Appl. Cryst., 2001, 34, 210-213.

29 A. C. Larson and R. B. Von Dreele, Los Alamos National Laboratory Report LAUR, 2000, 86-748.

30 R. D. Shannon, Acta. Crystallogr. A., 1976, 32, 751.

31 L. Xie, J. Ma, Z. Zhao, H. Tian, J. Zhou, Y. Wang, J. Tao and X. Zhu, Colloid. Surface. A., 2006, 280, 232–236.

32 D. Li, B. Dong, X. Bai, Y. Wang and H. Song, J. Phys. Chem. C., 2010, 114, 8219–8226.

33 C. Liu, Z. Xia, Z. Lian, J. Zhou and Q. Yan, J. Mater. Chem. C., 2013, 1, 7139.

34 Y. Huang, H. You, G. Jia, Y. Song, Y. Zheng, M. Yang, K. Liu and N. Guo, J. Phys. Chem. C., 2010, 114, 18051-18058.

35 D. Yang, G. Li, X. Kang, Z. Cheng, P. a. Ma, C. Peng, H. Lian, C. Li and J. Lin, Nanoscale., 2012, 4, 3450-3459.

36 C. Liu, Z. Xia, Z. Lian, J. Zhou and Q. Yan, J. Mater. Chem. C., 2013, 1, 7139.

37 M. Pollnau, D. R. Gamelin, S. R. Lüthi and H. U. Güdel, Phys. Rev. B., 2000, 61, 3337–3346.

38 Y. Li, G. Wang, K. Pan, B. Jiang, C. Tian, W. Zhou and H. Fu, J. Mater. Chem., 2012, 22, 20381.

39 F. Vetrone, J. Boyer, J. A. Capobianco, A. Speghini and M. Bettinelli, J. Appl. Phys., 2004, 96, 661.

40 D. Li, B. Dong, X. Bai, Y. Wang and H. Song, J. Phys. Chem. C., 2010, 114, 8219-8226.

41 D. Chen, L. Lei, J. Xu, A. Yang and Y. Wang, Nanotechnology., 2013, 24, 085708.

42 P. Haro-González, S. F. León-Luis, S. González-Pérez and I. R. Martín, Mater. Res. Bull., 2011, 46, 1051.

43 S. Zhou, K. Deng, X. Wei, G. Jiang, C. Duan, Y. Chen and M. Yin, Opt. Commun., 2013, 291, 138.

44 P. Du, L. Luo, W. Li and Q. Yue, J. Appl. Phys., 2014, 116, 014102.

45 X. Lü, Mater. Chem. Phys., 2005, 93, 526.

46 Y. Imai, R. Momoda, Y. Adachi, K. Nishikubo, Y. Kaida, H. Yamada and C. N. Xu, J.

Electrochem. Soc., 2007, 154, J77.

47 L. Zhang, H. Yamada, Y. Imai and C. N. Xu, J. Electrochem. Soc., 2008, 155, J63.

Table Caption

Table 1 Crystallographic data and structure refinement conditions for the BiT-0, BiT-0.05 and BiT-0.2.

Captions for figures

Fig. 1. (Color online) Room temperature XRD patterns of BiT-0 (a) and BiT-0.08 (b) synthesized at different temperatures.

Fig. 2. (Color online) Normalized monolog XRD plots of BiT-0 (a) and BiT-0.08 (b) ranging from 28.5^0 to 32.5^0.

Fig. 3. (Color online) SEM micrographs of BiT-0 synthesized at 500 (a), 600 (b), 700 (c), and 800 (d) ^oC.

Fig. 4. (Color online) Rietveld structural refinement results for BiT-0 (a), BiT-0.05 (b), and BiT-0.2 (c) nanoparticles. The cross dots represent the measured XRD reflections and the red solid lines are the Rietveld refined results. The green solid lines show the difference between the measured data and refined data. The short vertical solid lines correspond with the Bragg positions. The insets show a regionally enlarged drawing.

Fig. 5. (Color online) Measured UC spectra of BiT-0.08 at room temperature (a). The inset of

(a) gives the photograph of the UC luminescence of BiT-0.08. Integral intensities of UC green (b) and red (c) emissions versus t. The inset of (b) shows the UC spectra of Y_2O_3: Er and BiT-0.08 (sintered at 700 °C). Variation of $R_{R/G}$ as a function of t (d). The inset of (d) gives the FT-IR spectra of BiT-0.08.

Fig. 6. (Color online) UC spectra of BiT-x UCNPs at room temperature (a). Dependence of integral intensities of UC green (b) and red (c) emissions on x. $R_{R/G}$ as a function of x (d).

Fig. 7. (Color online) Calculated CIE chromaticity coordinates for BiT-0.02 (a), BiT-0.08 (b), and BiT-0.2 (c).

Fig. 8. (Color online) Dependence of lg(I/x) on lgx for the UC green emission of BiT-x

Fig. 9. (Color online) Dependence of UC green (a) and red (b) emission intensities on pumping power for BiT-0.08. The solid lines are the linear fitting results.

Fig. 10. (Color online) Energy-level diagram of the Er^{3+} ions and proposed UC mechanism schemes for BiT-x.

Fig. 11. (Color online) UC emission spectra of BiT-0.05 at 115 K, 145 K, 175 K, 205 K, and 235 K.

Fig. 12. (Color online) Normalized UC green emissions of BiT-0.05 at different temperatures (a). Natural logarithm plot of the FIR as a function of inverse absolute temperature (b). Temperature dependence of R in the range of 175 to 490K (c). S as a function of temperature (d).

Fig. 13. (Color online) UC emission spectra of BiT-0.05 under different immersion times. The inset gives the variation of emission intensity with immersion time.

Table 1. Crystallographic data and structure refinement conditions for the BiT-0, BiT-0.05, and BiT-0.2

Compound reference	0	0.05	0.2
Chemical formula	$Bi_4Ti_3O_{12}$	$Bi_{3.95}Er_{0.05}Ti_3O_{12}$	$Bi_{3.8}Er_{0.2}Ti_3O_{12}$
Formula mass	4686.432	4678.088	4653.056
Crystal system	orthorhombic	orthorhombic	orthorhombic
a (Å)	5.41195 (10)	5.40867 (10)	5.40482 (16)
b (Å)	5.44646 (10)	5.44238 (10)	5.43065 (16)
c (Å)	32.8075 (8)	32.8007 (7)	32.7991 (11)
Unit cell volume ($Å^3$)	967.032 (37)	965.523 (36)	962.706 (58)
Temperature	300K	300K	300K
Space group	Fmmm	Fmmm	Fmmm
No. of reflections	475	473	475
No. of data points	6699	6699	6699
Total refined variables	29	29	29
DWd	0.657	0.601	0.594
R_p(%)	3.71%	3.88%	4.03%
R_{wp}(%)	4.94%	5.15%	5.26%
Reduced χ^2	3.381	3.834	3.713

Fig.1

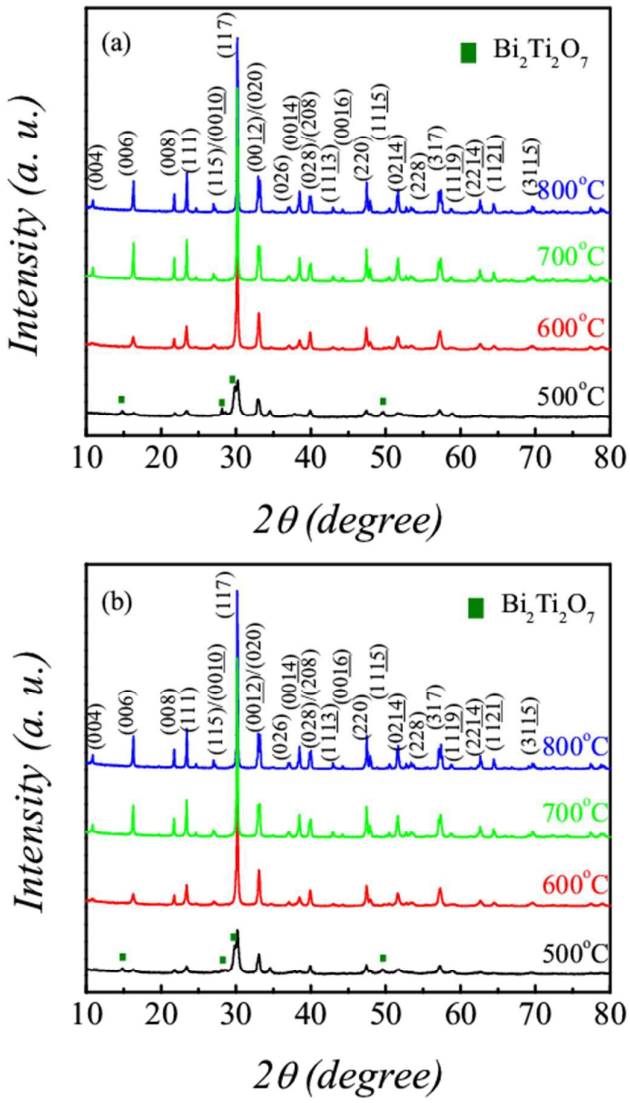

Fig. 2

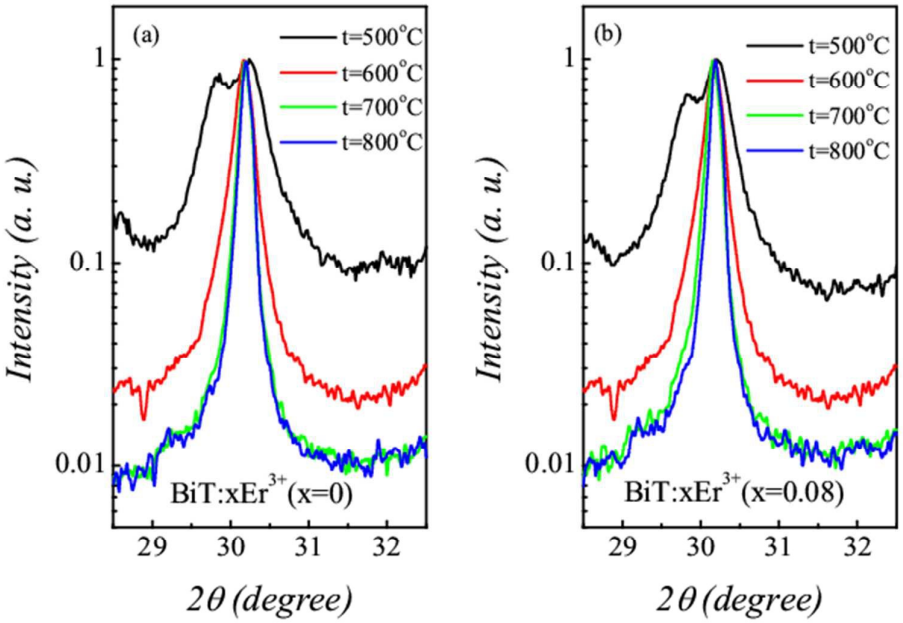

Fig. 3

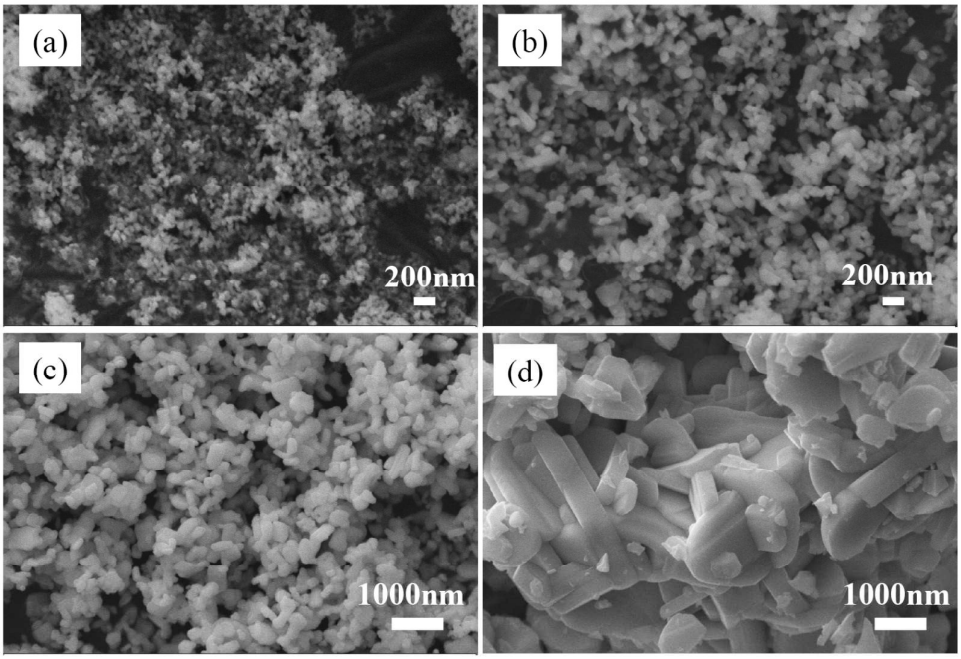

Fig. 4

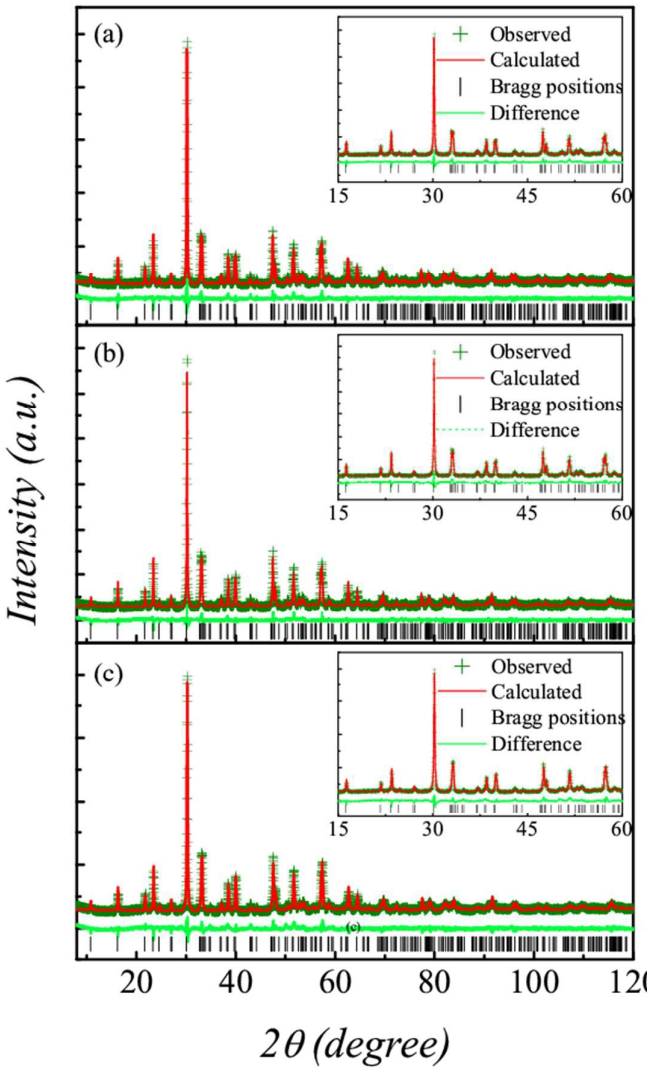

Fig. 5

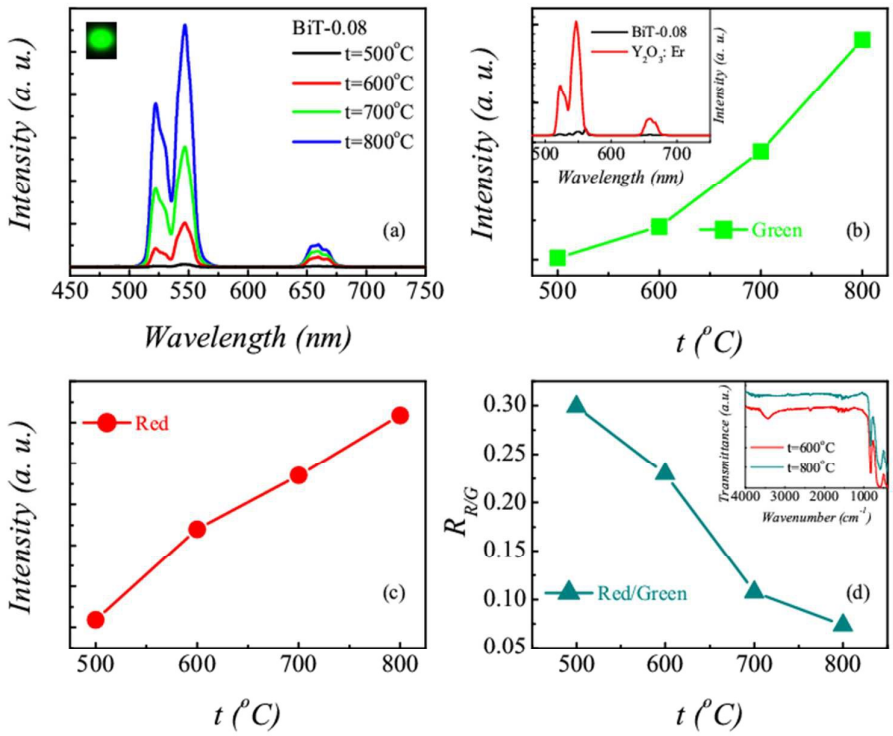

Fig. 6

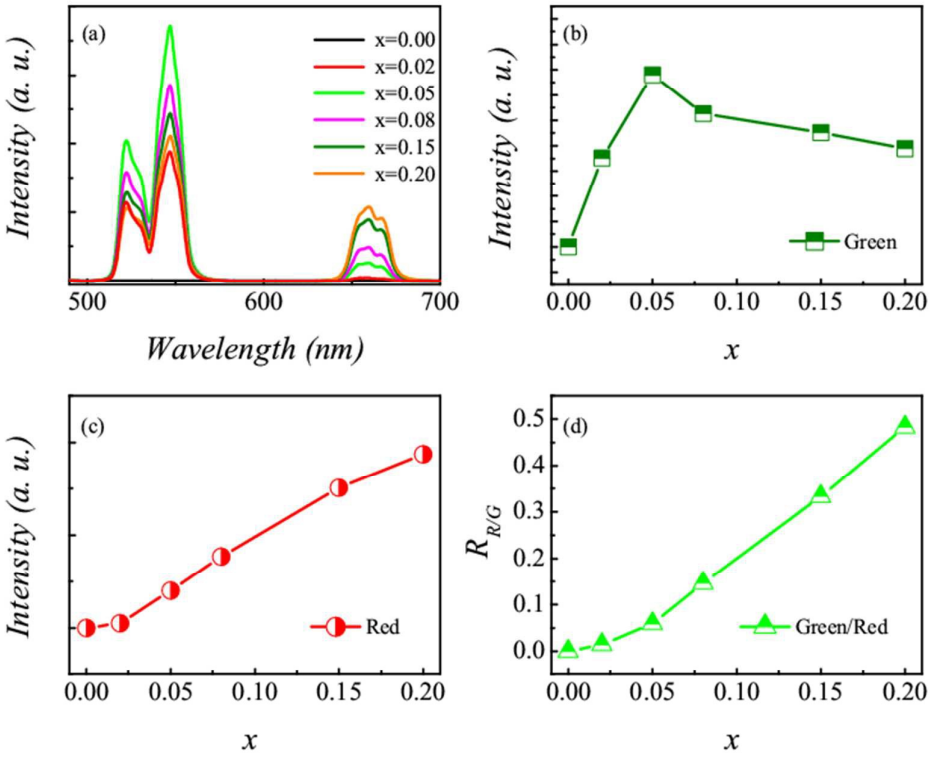

Fig. 7

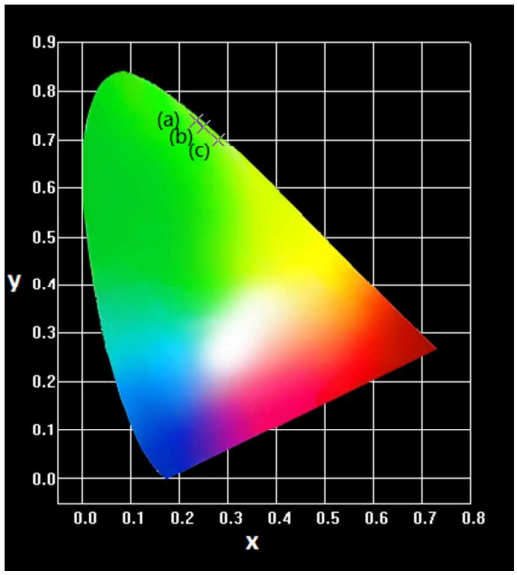

Fig. 8

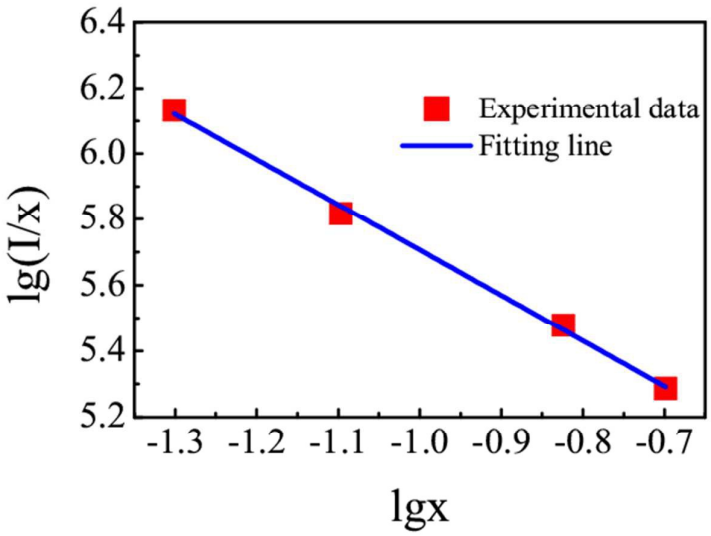

Fig. 9

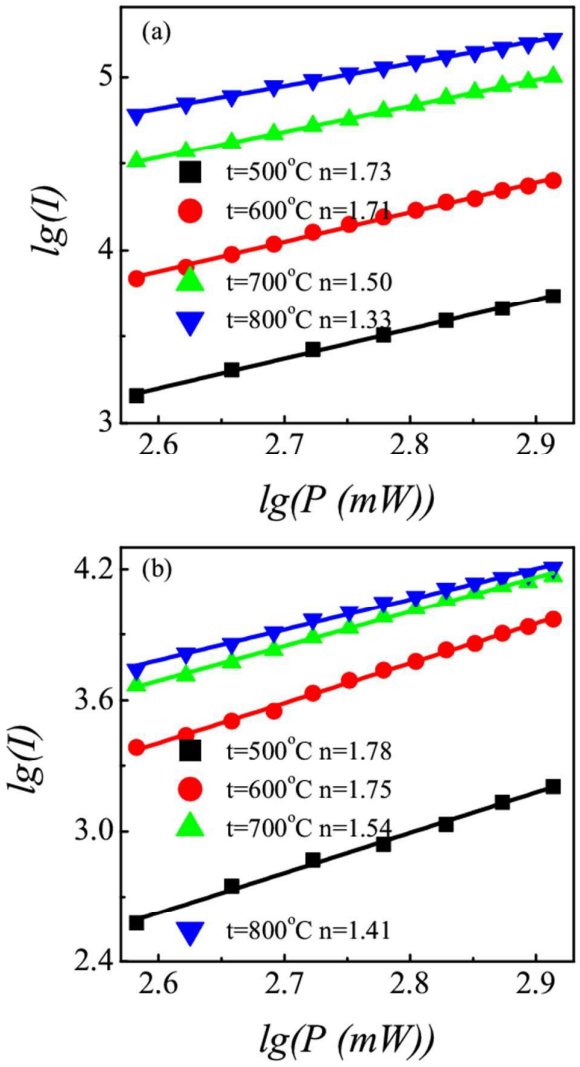

Fig. 10

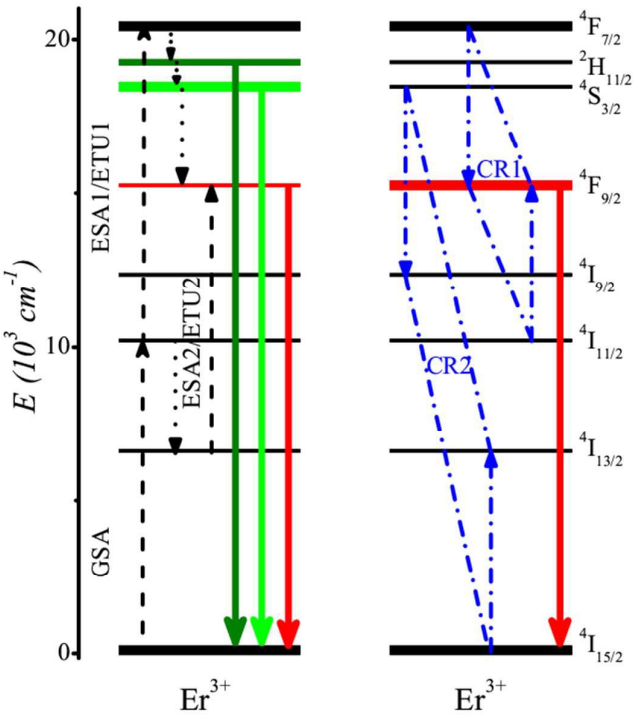

Fig. 11

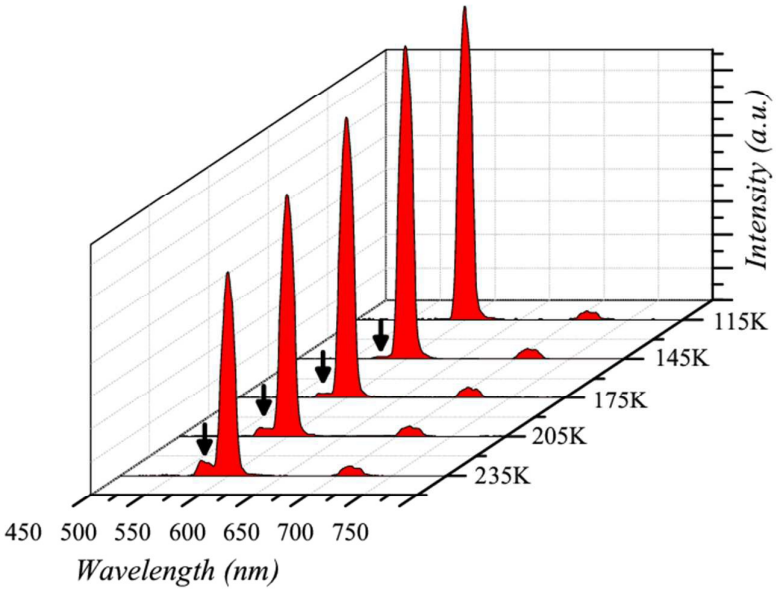

Fig. 12

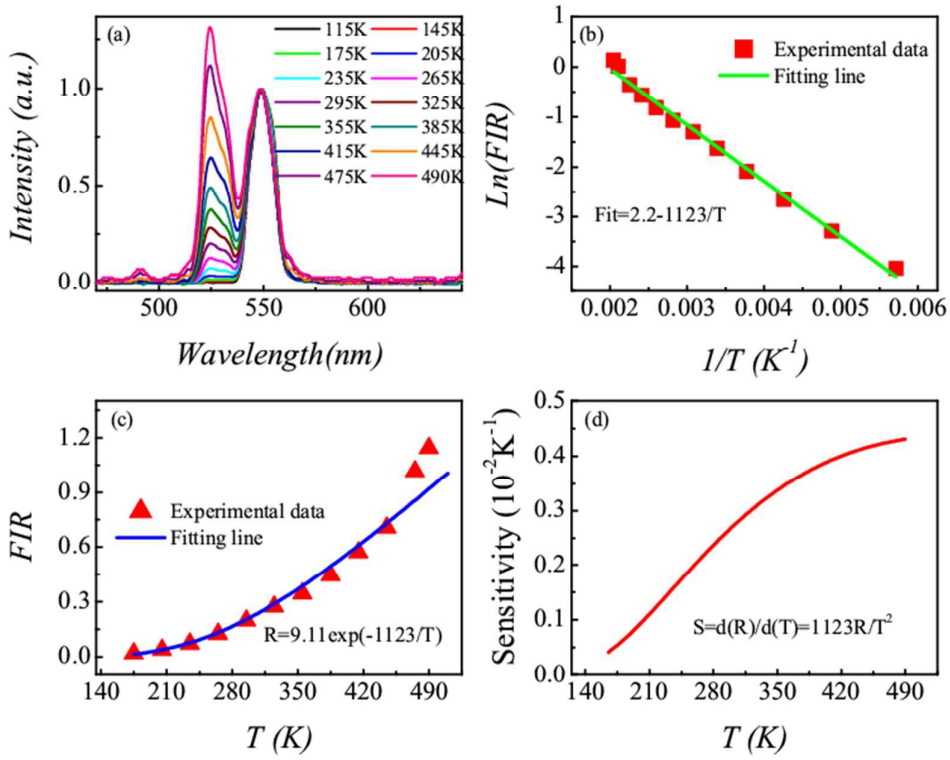

Fig. 13